Korean J. Chem. Eng., 39(9), 2523-2531 (2022)
DOI: 10.1007/s11814-022-1132-1

pISSN: 0256-1115
eISSN: 1975-7220

Direct fabrication of graphitic carbon nitride-wrapped titanate nanotube arrays toward photoelectrochemical water oxidation in neutral medium

Tho Truong Nguyen*, **Hong-Huy Tran**,*****, **Thi Minh Cao***, **and Viet Van Pham**,***,†**

*HUTECH University, 475A Dien Bien Phu Street, Binh Thanh District, Ho Chi Minh City, 700000, Vietnam
**Faculty of Materials Science and Technology, University of Science, VNU-HCM,
227 Nguyen Van Cu Street, District 5, Ho Chi Minh City, 700000, Vietnam
***Vietnam National University Ho Chi Minh City, Thu Duc City, Ho Chi Minh City, 700000, Vietnam

(*Received 22 December 2021 • Revised 10 March 2022 • Accepted 2 April 2022*)

Abstract−Realizing a long-term, high-performance, and affordable photocatalytic setting for water splitting processes remains challenging despite the tremendous promise. We present a direct fabrication of graphitic carbon nitride-wrapped titanate nanotube array (gC_3N_4-wrapped TNA) heterojunction photoelectrodes via a chemical vapor deposition-like process that leverages the pyrolysis and sublimation of melamine at 500 °C. The gC_3N_4-wrapped TNA heterojunction photoelectrodes show a 16 times enhancement of current density and photo-response than bare TNAs. Such a remarkable enhancement comes from the effective charge separation of the gC_3N_4/TNA interfaces, consequently accelerating water splitting to generate oxygen under visible light. In addition, our gC_3N_4-wrapped TNA photoelectrodes are developed under a neutral condition that significantly increases their widespread use for practical devices.

Keywords: TiO_2 Nanotube Arrays, Graphitic Carbon Nitride, Water Splitting, Water Oxidation, Pyrolysis Deposition

INTRODUCTION

Photoelectrochemical (PEC) water splitting to generate hydrogen and oxygen plays a central role in realizing our ambitious 2030 Sustainable Development Goals of energy efficiency and sustainable energy [1-5]. The origin of this remarkable progress comes from its sustainability, recyclability, low cost, and high energy conversion efficiency. However, it remains challenging to have a practically efficient energy conversion device.

Developing stable and high-performance photocatalytic materials for water splitting processes has been one of the most active research areas in this modern era. The astonishing performance generally comes from noble or rare materials [6-10]. However, such noble materials are rare and costly, undoubtedly hindering their widespread adoption in large-scale applications. Thus, several strategies have been implemented against the dependence of these noble and rare materials by using such materials in the form of single atoms or ultrathin layers [11-21]. Despite the possible reduction in the use of noble materials, these approaches inevitably consume an incredible total of noble materials, inadvertently affecting the goals for a sustainable nature.

Titanate nanotube arrays (TNAs) represent a unique class of photoelectrode materials for water splitting because of their highly oriented charge transport paths, significant specific surface areas, photo and chemical stability, slow charge recombination, ease of fabrication, and low cost [22-29]. Therefore, extensive approaches have been proposed to use TNAs as a photoelectrode for efficient water splitting. Such strategies include metal loading [30,31], doping [23, 32], bandgap engineering [33,34], narrow bandgap semiconductor coupling [35,36], and surface engineering [37,38].

Notably, coupling with metal-free graphitic carbon nitride (gC_3N_4) holds great potential for constructing practically efficient photoelectrodes. The origin for making such a combination to leap comes from the tremendous inherent advantage of gC_3N_4, showing an excellent visible light response, non-toxicity, low cost, and ease of manufacture [39-44]. Specifically, gC_3N_4/TNA heterojunction materials significantly improve PEC water splitting performance [45-47]. This remarkable combination originates from the proper bandgap configuration between TiO_2 and gC_3N_4. However, the documented performance of these gC_3N_4/TiO_2 heterojunctions is strictly constrained because of the low specific surface area and poor electrical conductivity of gC_3N_4 [48,49]. Additionally, the conventional approaches for fabricating these structures are complicated, laborious, poorly reproducible, and time-consuming, which hinders their potential for scalable manufacturing. In addition, reported studies mainly focus on alkaline media, which do not meet the practical conditions [50-53].

In this work, we directly fabricated gC_3N_4-wrapped TNA heterojunction photoelectrodes via a chemical vapor deposition-like process. We induced deposition of gC_3N_4 on the surface of TNAs through the melamine sublimation at 500 °C. The as-obtained gC_3N_4-wrapped TNA photoelectrodes show an excellent photoresponse ability because of their enhanced charge density and effectively prolonged charge recombination, indicating an improvement in water splitting under visible light. Also, our gC_3N_4-wrapped TNA photoelectrodes are developed under neutral conditions, which has practical significance in the environmental and economic advantages.

---

†To whom correspondence should be addressed.
E-mail: pvviet@hcmus.edu.vn

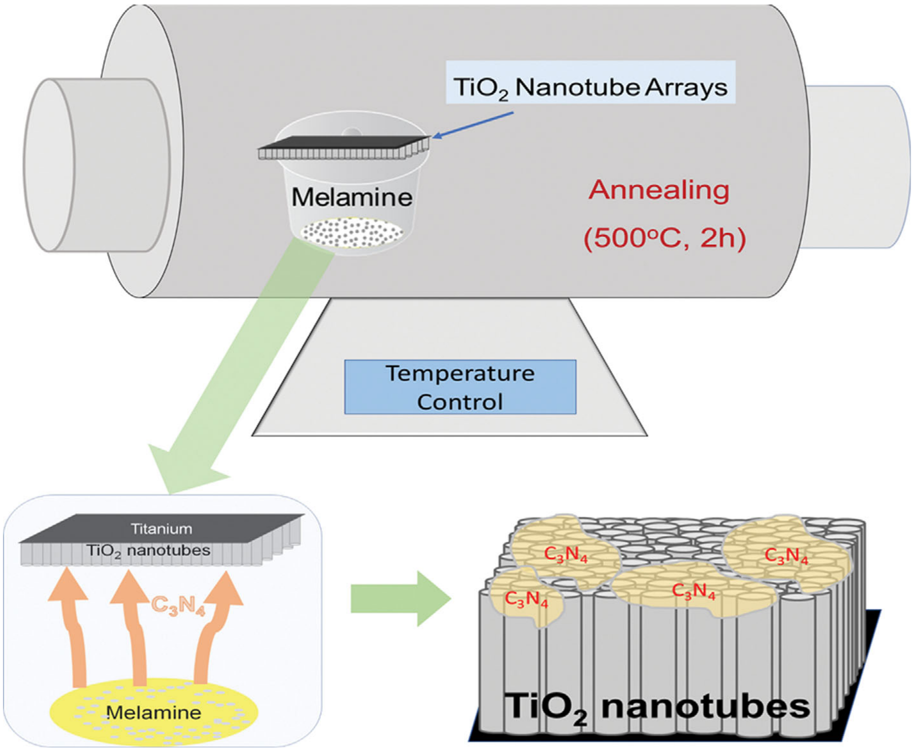

Scheme 1. A schematic illustration of the deposition of gC_3N_4 onto TNA photoelectrodes. The objects are not drawn to scale for clarity.

EXPERIMENTAL

1. Chemicals and Materials

Titanium (Ti) foils with a thickness of 0.125 mm were provided by Alfa Aesar (USA). Sodium hydroxide (NaOH, 99%, Fisher chemical, USA), hydrochloric acid (HCl, 36.5%, Fisher chemical, USA), acetone (C_3H_6O, Fisher BioReagents, USA), and absolute ethanol (C_2H_5OH, Fisher BioReagents, USA) were used to clean the surface of Ti foils. Ethylene glycol ($C_2H_6O_2$, 99%, Fisher Chemical, USA), deionized water (DI) (MilliQ, 18 MΩ cm^{-1}), and ammonium fluoride (NH_4F, 96%, Fisher Chemical, USA). Melamine ($C_3H_6N_6$), $K_2Cr_2O_7$, and KI chemicals were provided by Acros Organics (USA) with a purity of 99%.

2. Preparation of Materials

Preparation of TNAs: Highly ordered TNAs were prepared via a two-step anodization oxidation process [54]. Briefly, the Ti foils were cut into 1 cm×2 cm pieces and polished by sandpaper (Kovax P1000), followed by immersing in 10% HCl and 12 M NaOH solutions, respectively, to remove surface contaminants. Next, these Ti pieces were sonicated in acetone, ethanol, and DI water, respectively, followed by a drying step at 60 °C for 30 min. The electrolyte solution was prepared by dissolving 0.25 g NH_4F in 4.5 mL DI water. Then, 40.5 mL of ethylene glycol was added with continuous stirring for 15 min. Anodic oxidation was performed in a two-electrode electrochemical cell in a Teflon-lined steel reactor. The Ti foil and Pt wire were used as anode and cathode, respectively. In the first anodic oxidation cycle, the Ti foil was applied a DC voltage of 30 V for 2 h, resulting in TiO_2 and partly developed TNAs on the surface of Ti pieces. Next, this surface was treated with sonication in a DI water medium for 10 min, removing the unnecessary oxide layer and leaving nucleation sites for the later growth of TNAs. The surface was then ready for the second anodic oxidation cycle at the same voltage for 30 min. Commonly, the sample was rinsed with DI water after the anodization process, followed by drying and annealing steps at 60 °C and 500 °C for 2 h, respectively.

Preparation of gC_3N_4-wrapped TNA photoelectrodes: gC_3N_4-wrapped TNAs were fabricated through a chemical vapor deposition-like process based on the pyrolysis of melamine, as illustrated in Scheme 1. Briefly, 0.3 g of melamine was placed in a crucible together with a TNA photoelectrode, covering the surface of melamine (Scheme 1). A hole with a diameter of 6 mm was drilled on the lid of the crucible where the TNA was positioned, followed by an annealing process at 500 °C for 2 h.

3. Characterizations of Materials

Fourier transform infrared spectrophotometer (FTIR) analysis was studied in the range of 400-4,000 cm^{-1} using a JASCO V4700 to investigate molecular vibrations of the materials. The material layer was collected from the Ti substrate, then mixed with KBr at a 1/300 (sample/KBr) ratio. The sample was prepared by molding it into a pellet shape with a diameter of 1 cm. X-ray diffraction (XRD) patterns were used to determine the materials' phase composition and crystal structure using a Bruker D8 X-ray diffractometer with the Cu K radiation (λ=0.154064 nm) and the scanning rate of 0.02° min^{-1} in the 2θ range of 10°-80°. The surface morphology of the materials was observed by scanning electron microscope (SEM) images, captured on a Hitachi SEM Hitachi S4800 at an accelerating voltage of 10 kV. The X-ray photoelectron spectra (XPS) were conducted on a PHI Hybrid Quantera photoelectron spectrometer, using a monochromate 450 W Al Kα source as the exciting source.

4. Photoelectrochemical Water Oxidation Properties of Materials

The PEC water splitting of the materials was studied in a neutral medium, using a three-electrodes PEC cell on a Biologic SP-200 (France). The as-prepared materials were used as a working electrode, Pt wire was used as a counter electrode, and Ag/AgCl 3 M NaCl were reference electrodes. A 1 M Na_2SO_4 (pH 7.4) solution was used as the electrolyte solution. The light source was provided by a solar simulator lamp, ABET Instruments, using a Xenon lamp with a power of 150 W. A UV filter was used to leave only the visible light passing. The potential V vs. Ag/AgCl was converted into a V vs. RHE relation using the Nernst equation (Eq. (1)).

$$E_{RHE}=E_{Ag/AgCl}+E_{0\,(Ag/AgCl)}+0.059\times pH \tag{1}$$

where $E_{0\,(Ag/AgCl)}=0.210$ V at 25 °C, a pH value of 7.4 was recorded for the electrolyte solution.

The linear sweep voltammogram (LSV) analysis of the as-prepared materials was recorded by observing the current density vs. the applied linear potential in the range of −1 to 1 V vs. Ag/AgCl in a neutral medium. The photo-response ability of the materials was captured by applying a potential voltage of 0 V vs. Ag/AgCl under repetitive on-off illumination conditions.

Mott-Schottky plots were obtained at a frequency of 1 kHz, amplitude of 10 mV, in the potential range of −1 to 1 V vs Ag/AgCl. The flat band potential is generally obtained from capacitance versus voltage (CV) measurements. The observed capacitance values are subsequently incorporated into the following Mott-Schottky equation to evaluate the flat band potential, according to Eq. (2) [55]:

$$\frac{1}{C^2}=\frac{2}{\varepsilon\varepsilon_0 A^2 q N_d}\left(V-V_f-\frac{k_B T}{q}\right) \tag{2}$$

where, C is the semiconductor/metal or semiconductor/electrolyte junction capacitance, ε is the dielectric constant of semiconductor, V is the applied potential, V_f is flat band potential, N_d is doping density, A is the area of the depletion region/space charge region, k_B is Boltzmann's constant, T is the absolute temperature at which the measurement is performed. The above equation plot yields a straight line from which the flat band potential V_f of a given semiconductor can be extracted.

RESULTS AND DISCUSSION

1. Material Characterization

Fig. 1 shows the diffraction peaks of TNAs at $2\theta=25°$, 47.16°, and 70.05°, characterized by the (101), (200), and (220) lattice planes of anatase phase TiO_2, respectively (JCPDS No. 21-1272). In addition, the diffraction peak recorded at $2\theta=37.27°$ represents the (100) lattice plane of the titanium substrate. The XRD pattern of gC_3N_4 presents two characteristic peaks at $2\theta=13.1°$ and 27.9°, corresponding to the (100) and (002) planes of gC_3N_4, respectively (JCPDS 87-1526). Also, these two peaks are attributed to the in-plane structure of tri-s-triazine units and the interlayer stacking of conjugated aromatic groups in gC_3N_4. For the gC_3N_4-wrapped TNA sample, the presence of, at the same time, typical diffraction peaks of gC_3N_4 and TNAs is observed, indicating the success in making gC_3N_4/TNA composites. The diffraction peak intensity of gC_3N_4 in the gC_3N_4-wrapped TNA sample is relatively low, likely due to the low concentration of gC_3N_4 introduction in the heterojunction. Such a combination also induces a change in the crystal orientation of the composite where the (220) lattice plane is the most oriented. The difference in crystallinity of TiO_2 materials after combining with other materials to form heterojunctions was previously observed because the formation of this heterojunction structure relates to the competitive growth between component materials [56,57].

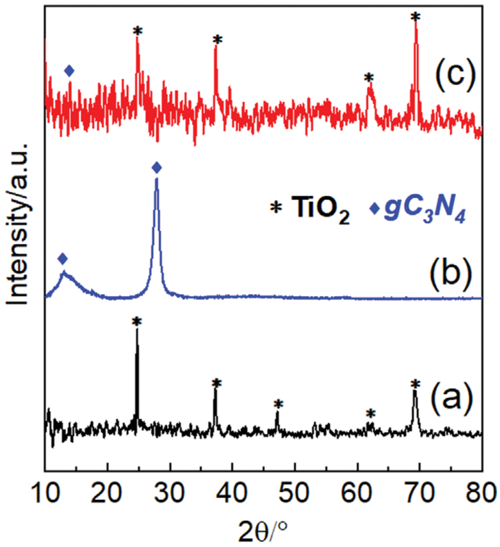

Fig. 1. XRD patterns of TNA (a), gC_3N_4 (b), and gC_3N_4-wrapped TNA samples (c).

The compositional information and chemical bonds of TNA, gC_3N_4, and gC_3N_4-wrapped TNA samples are characterized by FTIR spectroscopy. In Fig. 2(a), the typical peaks in the region from 450 cm^{-1} to 750 cm^{-1} for TNAs are attributed to Ti-O-Ti and Ti-O stretching vibration modes in anatase TiO_2 crystals. The formation

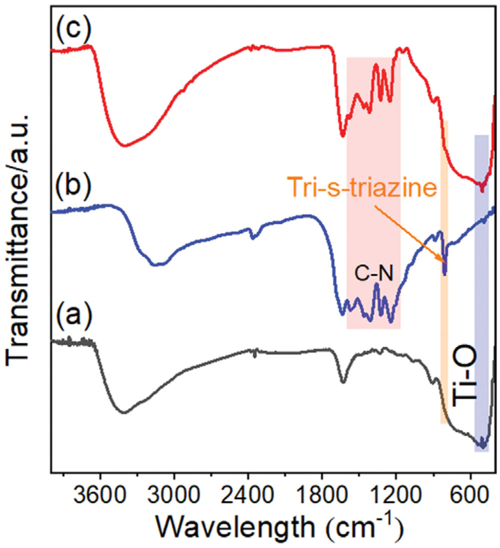

Fig. 2. FTIR spectra of TNAs (a), gC_3N_4 (b), and gC_3N_4-wrapped TNAs (c).

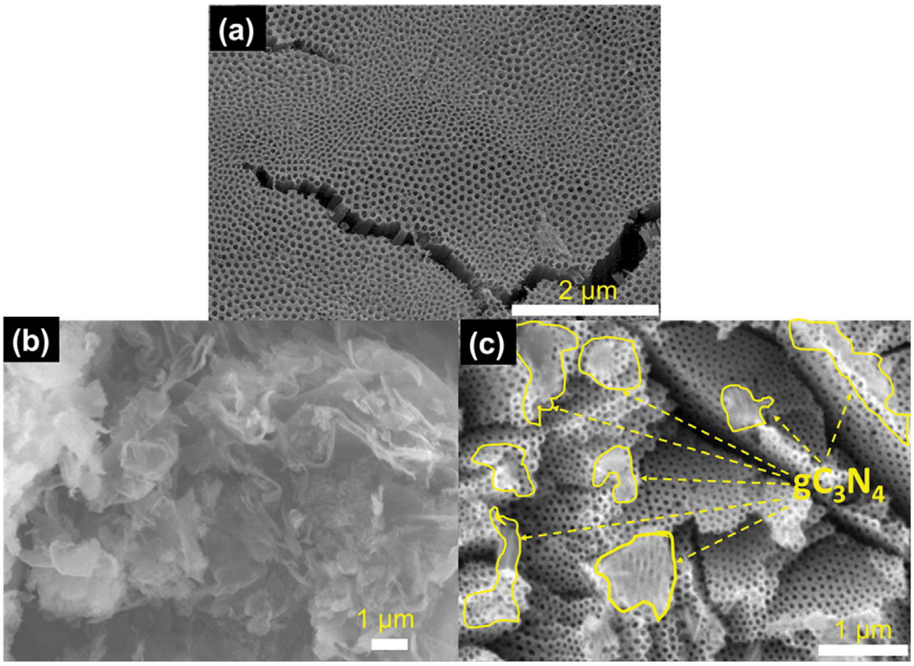

Fig. 3. SEM images of TNAs (a), gC_3N_4 (b), and gC_3N_4-wrapped TNAs (c).

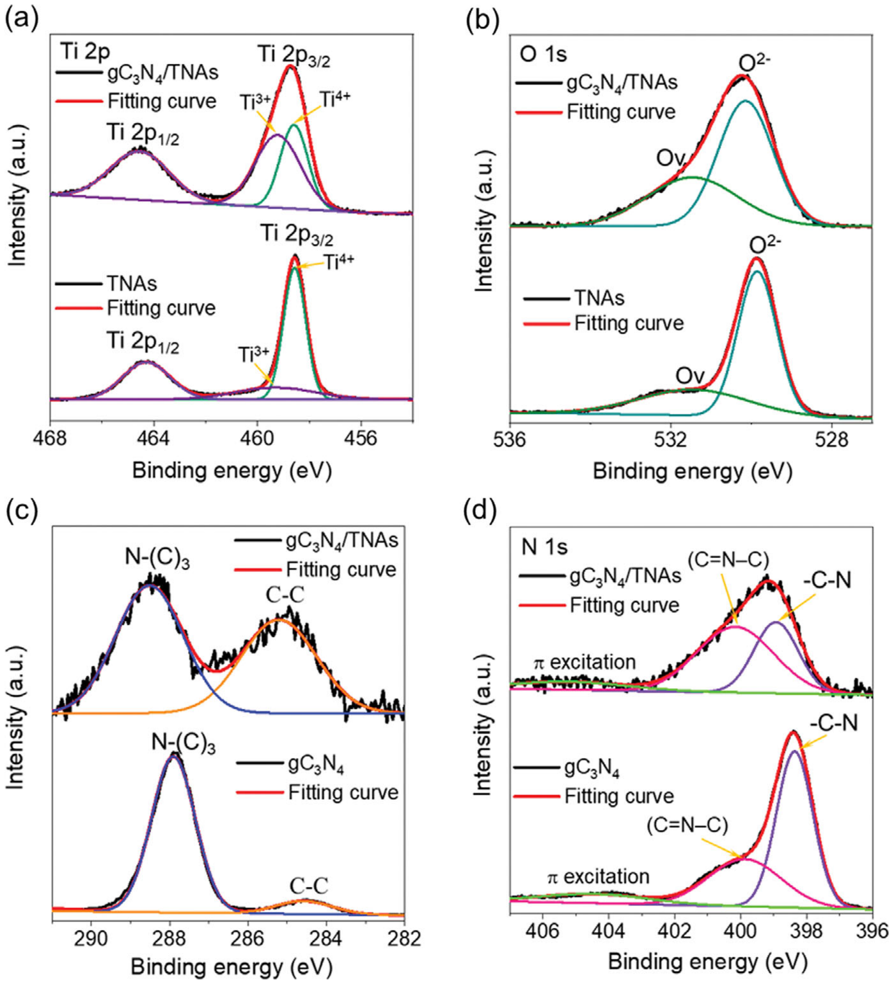

Fig. 4. High resolution XPS of Ti 2p (a), O 1s (b), C 1s (c), and N 1s (d).

of the gC_3N_4 material is characterized through C-N oscillation states ranging from 1,200 to 1,640 cm^{-1} (Fig. 2(b)). Besides, a sharp peak at 809 cm^{-1} is attributed to the characteristic breathing mode of tris-triazine units. Furthermore, the FTIR result of the gC_3N_4-wrapped TNA in Fig. 2(c) has given the most distinctive peaks of gC_3N_4 and TiO_2. The coexistence of TiO_2 and gC_3N_4 in gC_3N_4-wrapped TNA heterojunction is thus confirmed.

The morphology of the materials is captured via SEM images, as shown in Fig. 3. After the two steps of the anodic oxidation process, the surface of the Ti foil is densely covered by hollow nanostructures with uniformity in diameter size (~75 nm), as shown in Fig. 3(a). Specifically, the nanotubes arrange closer to each other, eliminating the cavities between nanotubes. Fig. 3(b) shows the morphology of the gC_3N_4 after an annealing process at 500 °C, generally having a sheet-like structure. Upon being combined by our chemical vapor deposition-like process, the surface of the TNAs is wrapped by gC_3N_4 sheets, as shown in Fig. 3(c). In addition, this result shows a significant change of the morphology of the TNAs upon being combined with gC_3N_4.

The high-resolution XPS (HR-XPS) spectra are recorded to accurately analyze the surface chemical composition and valence state of the elements in the as-obtained materials. Fig. 4(a) shows the HR-XPS of the Ti 2p orbital; three deconvoluted peaks at 462.40, 457.42, and 456.68 eV are observed for the TNAs sample, indicating Ti $2p_{3/2}$, Ti^{3+}, and Ti $2p_{1/2}$ states, respectively [58]. This result indicates that the oxidation state of Ti ions is not wholly Ti^{4+} since there is a small amount of Ti^{3+} states. The HR-XPS Ti 2p profile of the gC_3N_4-wrapped TNAs sample shows a slight shift toward higher binding energies, suggesting a possible migration of electrons from the gC_3N_4 to TNAs [59]. Total area percentages of fitting spectra for Ti 2p in TNAs and gC_3N_4/TNAs are shown in Table 1. Briefly, the total area percentage of Ti $2p_{3/2}$ peak in TNAs is 51.68%, while gC_3N_4/TNAs is only 27.44%. In the reverse direction, the total area percentage of Ti^{3+} in TNAs is 17.0%, but considerably increased to 38.8% in the gC_3N_4/TNAs. However, the density of Ti $2p_{1/2}$ remains unchanged. The total area percentage of Ti $2p_{1/2}$ in TNAs is 31.32 and is 33.74% in gC_3N_4/TNAs. These results indicate the migration of electrons from gC_3N_4 to TNAs, causing a additional reduction of Ti^{4+} to Ti^{3+}.

Table 1. Percentage of the total area for Ti 2p, Ti^{3+} in TNAs and gC_3N_4/TNAs

Sample	Peak area by integrating data (%)		
	Ti $2p_{3/2}$	Ti $2p_{1/2}$	Ti^{3+}
TNAs	51.68	31.32	17.0
gC_3N_4/TNAs	27.44	33.74	38.82

O 1s peaks are recorded at 529.8 and 531.5 eV for the TNAs sample (Fig. 4(b)), which are typically assigned to the lattice oxygen (O^{2-}) and oxygen vacancies (O_v) in TiO_2 materials [60]. However, the peak of O^{2-} shifts to higher binding energy, located at 530.1 eV, suggesting an interfacial interaction between TNA and gC_3N_4. In the HR-XPS C 1s profiles of the obtained materials, two typical peaks are observed at 284.6 and 287.9 eV, presenting the C-C and N-$(C)_3$ bonds, respectively (Fig. 4(c)) [61]. In addition, the N 1s peaks of sp^2 -hybridized aromatic N(C=N-C) (398.4 eV) and C-N-H groups (399.9 eV), as shown in Fig. 4(d). However, these peaks show an apparent shift toward higher binding energies. Precisely, the shifted peaks are located at 285.2 eV for C-C, 288.5 eV for N-$(C)_3$, 398.9 eV for N(C=N-C), and 400.2 eV for C-N-H. These observations strongly support the hypothesis on the migration of electrons from gC_3N_4 to the TNAs, leading to decreased electron density. Thus, the HR-XPS results indicate the strong interaction between TNAs and gC_3N_4 at the interface. This evidence has clearly shown the formation of the heterostructure gC_3N_4-wrapped TNAs. The results present a remarkable agreement between the characterization results, clearly indicating the successful fabrication of the gC_3N_4-wrapped TNA nanocomposites via our direct chemical vapor deposition-like process.

2. Photoelectrochemical Water Oxidation Ability in the Neutral Medium of gC_3N_4-wrapped TNAs

The LSV in the dark and under the illumination of the materials is explored for the oxygen evolution reaction (OER) studies with a three-electrode electrochemical cell in 1 M Na_2SO_4 solution at a pH of 7.4 (Fig. 5(a)). The difference of TNAs with the thermal treat-

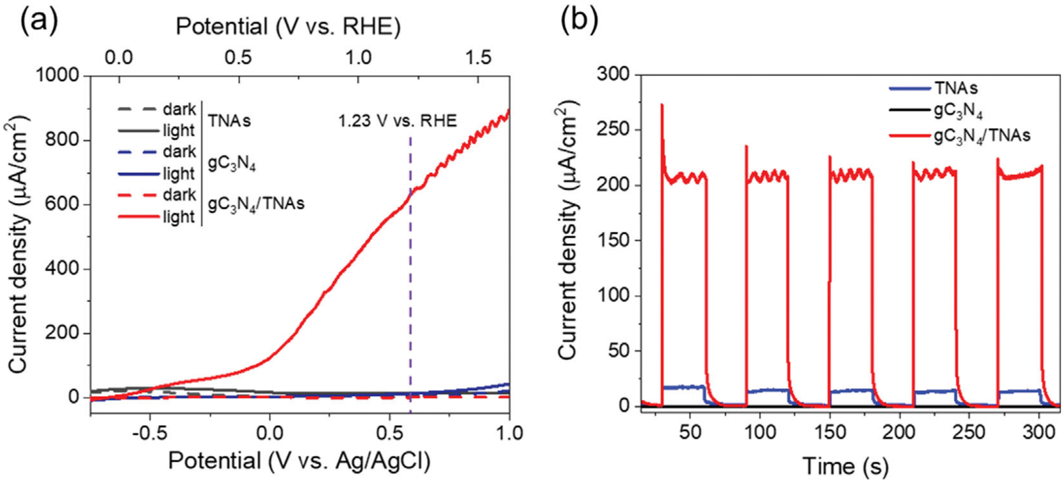

Fig. 5. LSV of materials (a), and photocurrent density of materials at 0.63 V vs. RHE (b) in 1M Na_2SO_4 electrolyte (pH 7.4).

Table 2. A comparison of photocurrent on this work with other publications

Electrode materials	Method	Morphology of materials	Applied potential	Electrolyte	pH medium	Current density (μA/cm^2)	Ref.
g-C_3N_4/TiO_2	Thermal decomposition	Nanosheets/ Nanotube arrays	0 V vs. SCE	0.5 M Na_2SO_4	Not provided	1.79	[65]
Pt/g-C_3N_4/TNTs	Chemical vapor deposition	Nanosheets/ Nanotube arrays	0.75 V vs. Ag/AgCl	0.1 M Na_2SO_4	Not provided	10	[65]
g-C_3N_4/TNAs	Electrochemical	Nanosheets/ Nanotube arrays	0 V vs. SCE	0.5 M Na_2SO_4	Not provided	4	[66]
g-C_3N_4/TiO_2	Electrodeposition	Nanosheets/ Nanotube arrays	1 V vs. Ag/AgCl	1 M Na_2SO_4	Not provided	140	[67]
g-C_3N_4/Pt/TiO_2	Chemical adsorption and calcination	Nanosheets/ Spheres	-	1 M Na_2SO_4	Not provided	0.08	[68]
g-C_3N_4/TiO_2	Microwave-heating technique	Nanoparticles/ Nanocorns	-	0.5 M Na_2SO_4	Not provided	6.8	[69]
g-C_3N_4/TNAs	Thermal decomposition	Nanosheets/ Nanotube arrays	0.63 V vs. RHE	1 M Na_2SO_4	7.4	206	This study

ment at 500 °C and TNAs without the thermal treatment has also been indicated as in Fig. S1. In detail, the photoresponse ability of TNAs without thermal treatment has a current density of 2.87 μA/cm^2, while that of TNAs 500 °C is around 17.51 μA/cm^2 in the first cycle of irradiation. Therefore, we conducted investigations of TNAs 500 °C sample in the experimental works. As in Fig. 5(a), the current density of the materials under dark conditions is negligible. However, under the illumination, all the materials present the ability to generate current. Specifically, under the illumination and the applied potential scanned from –0.37 V vs. RHE to 1.63 V vs. RHE, the PEC ability of the gC_3N_4-wrapped TNAs presents the highest value. The onset potential of TNAs is obtained at −0.22 vs. RHE, and the current density at the highest applied potential value is about 14 μA/cm^2. The onset potential of gC_3N_4 is about –0.07 V vs. RHE, and the current density at the highest applied potential value is about 43.3 μA/cm^2. A superior OER activity is recorded over the gC_3N_4-wrapped TNAs sample. In detail, the onset potential of gC_3N_4-wrapped TNAs is obtained around −0.05 V vs. RHE. The current density slope is enormously increased from 0.6 V vs. RHE and linear to the applied potential. At 1.63 V vs. RHE, the current density of gC_3N_4-wrapped TNAs can reach around 895.1 μA/cm^2, 64 and 21 folds higher than that of the TNAs and gC_3N_4 samples, respectively (Fig. 5(a)). This result means that the charge recombination is hindered by accelerating the electron's transfer. In addition, at the applied potential of 1.23 V vs. RHE, which is known as E_0 for splitting O_2 from H_2O (at pH 0), the gC_3N_4-wrapped TNAs sample expresses a current density of 635.1 μA/cm^2, indicating a strong performance in PEC in comparison with the single-component samples. By these results, the increase of carrier concentration after creating the interface between gC_3N_4 and TNAs is achieved.

The photo-response ability of the materials under visible light is shown in Fig. 5(b). The discontinuity cycle of the illumination is kept at 30 s. The interaction of the materials to the visible light is obtained through the difference of current density under on-off operations. As shown in Fig. 5(b), the current density of the TNAs sample under irradiation is about 4.3 μA/cm^2. In contrast, that of gC_3N_4 is very low, just about 1 μA/cm^2. However, the formation of gC_3N_4-wrapped TNAs heterojunctions strongly enhances the photocurrent density. The current density of the gC_3N_4-wrapped TNAs is obtained at about 274.1 μA/cm^2 in the early stage of illumination and kept stable at around 206 μA/cm^2 even after five cycles. This result is still 48-fold higher than that of the TNAs sample. This result again demonstrates the success in increasing the carrier concentration and amending the recombination of e^- - h^+ in the heterojunction. Such an observation is already evidenced from the XPS results, leading to an increase in the current density and likely enhancing the PEC performance. A comparison is made to demonstrate the improvement in PEC performance of the gC_3N_4-wrapped TNAs heterostructure in our work, as shown in Table 2. In addition, the effect of sacrifical agents (s.a.) to the PEC activities of materials was investigated to determine the role of carriers in the catalysis process. In detail, we used 0.1 mM of $K_2Cr_2O_7$ and KI as scavenger agents of photogenerated e^- and h^+, respectively, to add the Na_2SO_4 1 M electrolyte solution in the photocatalytic reaction [62,63]. The results of the effect of the s.a. are indicated in Fig. S2(a). Therein, the LSV of gC_3N_4/TNAs with the presence of KI in the electrolyte displays a low current density. At 1.23 V vs. RHE, the current density under irradiation is only around 41.5 μA/cm^2. This result indicates the importance of h^+ in the OER process of PEC water splitting. Otherwise, LSV of gC_3N_4/TNAs with the presence of $K_2Cr_2O_7$ in the electrolyte shows a strongly enhanced current density in comparison with that of normal electrolyte. Fig. S2(b) shows the current density at an applied potential of 1.23 V vs. RHE under irradiation can reach to 975.4 μA/cm^2. The improvement in current density is explained due to the presence of scavenger agent, which reduces the recombination of e^- - h^+ pairs. In addition, maximum photocurrents are also affected by the presence of the $K_2Cr_2O_7$ as a strong h^+ donor agent, leading to enhance OER process in PEC water splitting [64].

The Mott-Schottky plot is considered an effective method to ana-

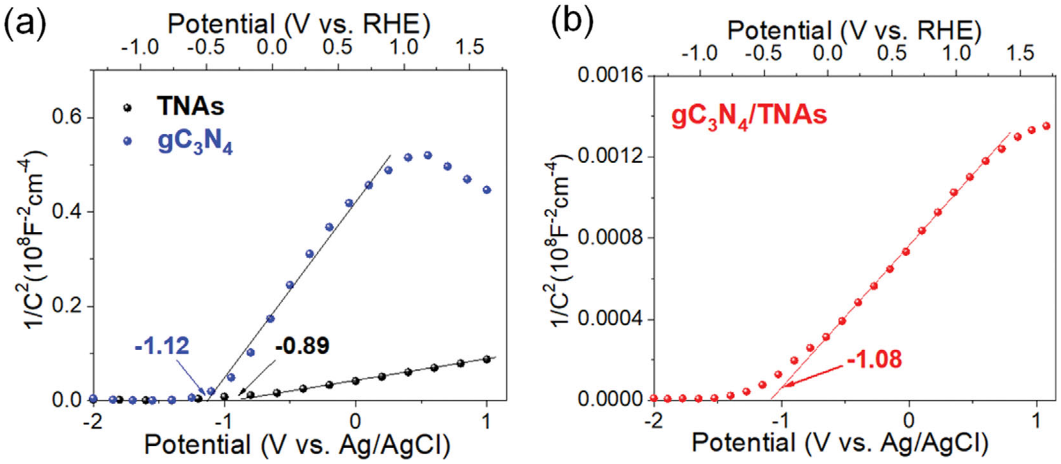

Fig. 6. Mott-Schottky plots of TNAs, gC_3N_4 (a) and gC_3N_4-wrapped TNA (b).

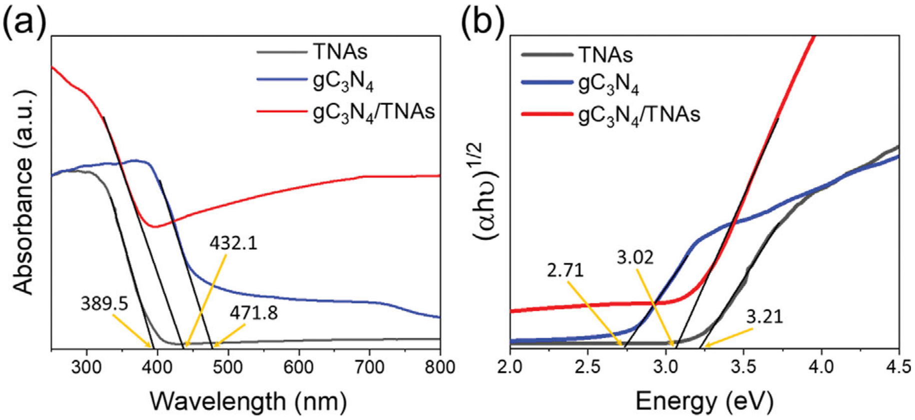

Fig. 7. DRS spectra (a) and Tauc plots (b) of materials.

lyze the electrochemical properties of materials, the behavior of the carriers, states of the semiconductor materials. As shown in Fig. 6, the Mott-Schottky plots of all materials in this contribution have been obtained through positive slopes. This indicates that all samples pose n-type semiconductor properties.From the Mott-Schottky results in Fig. 6 and according to Eq. (2), the CB levels of the materials are obtained at –0.31 V vs. RHE, –0.47 V vs. RHE, and –0.45 V vs. RHE for TNAs, gC_3N_4 and gC_3N_4-wrapped TNAs, respectively. As shown in Fig. 6(a), the CB of gC_3N_4 is much higher than that of TNAs. This could promote the e^- migration from gC_3N_4 to the TNAs. As shown in Fig. 6(b), the CB of gC_3N_4-wrapped TNAs is shifted to a higher level than TNAs. Besides, the intensity of $1/C^2$ slope of gC_3N_4-wrapped TNAs is much lower than that of TNAs and gC_3N_4, indicating a higher charge storage capacity. A smaller slope suggests that the gC_3N_4-wrapped TNAs sample has a higher carrier density and much faster carrier transfer, agreeing with the PEC results. This evidence has proven the richness of e^- after creating the heterojunction.

To evaluate the interaction of the materials with radiation, DRS spectra and Tauc plots of the materials were obtained and shown in Fig. 7. As can be seen in Fig. 7(a), the TNAs sample is only activated in the UV range, which is demonstrated through an absorption edge at 389.5 nm in the DRS result. Besides, the DRS spectrum of gC_3N_4 shows an absorption edge.

In contrast, the gC_3N_4 material shows an absorption edge at 471.8 nm, which allows gC_3N_4 to perform photocatalytic reactions in the visible light region. Moreover, for this reason, gC_3N_4 is considered as a potential candidate for modification of pristine TiO_2 material to form a heterostructure that could enhance optical interaction. This phenomenon is indicated by the DRS spectra of gC_3N_4/TNAs heterostructure. The absorption band edge is shifted to 432.1 nm compared to pristine TNAs. Furthermore, the absorbance of gC_3N_4/TNAs in the range after 432.1 nm is also higher than that of TNAs and gC_3N_4, which allows this heterostructure to enhance photoelectrochemical water splitting signals. To evaluate the optical bandgap energy for the indirect bandgap semiconductor, such as TiO_2 and gC_3N_4, Tauc plots of the materials are extrapolated through the Eq. (3) and shown in Fig. 7(b) [70].

$$\alpha hv = A(hv - Eg)^{1/2} \tag{3}$$

The bandgap of TNAs, gC_3N_4, and gC_3N_4/TNAs is calculated at about 3.21 eV, 2.71 eV, and 3.02 eV, respectively. As can be seen, the bandgap of gC_3N_4/TNAs is strongly reduced compared to that of TNAs. These results have demonstrated the efficiency in the modification of TNAs by gC_3N_4.

We have successfully obtained a gC_3N_4-wrapped TNA photoelec-

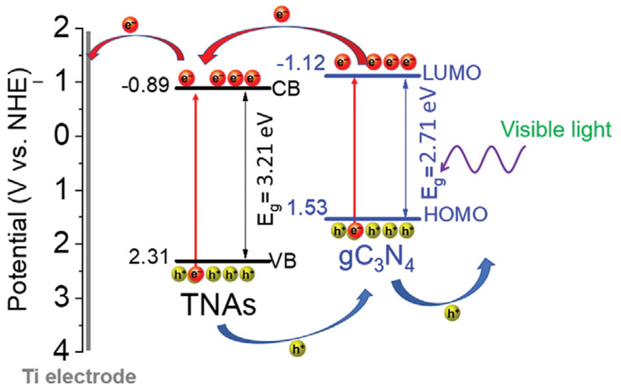

Fig. 8. Schematic illustration of charge transfer pathway in gC_3N_4-wrapped TNAs heterojunction for water oxidation activity.

trode based on the presented results, showing excellent water oxidation in a neutral medium under visible light. The enhanced water oxidation originates from efficient charge separation because of the formed interface between gC_3N_4 and TNA through the chemical vapor deposition-like process. Based on the Mott-Schottky plots and Tauc plots, a proposition of possible mechanism for the photocatalytic water oxidation of the gC_3N_4-wrapped TNAs has been shown in Fig. 8. Because the conduction band (CB) position of the gC_3N_4 is more negative than that of the TiO_2 [41,71], an internal local electric field is formed. This phenomenon induces the migration of photogenerated electrons from the CB of gC_3N_4 to the TNAs and the Ti electrode, which contributes significantly in the PEC activity of gC_3N_4-wrapped TNAs (as in Fig. S2). Spontaneously, the holes in the valence band (VB) of the TNAs transfer to the VB of the gC_3N_4, which readily oxidize the surrounding water and leads to efficient charge separation and effective water splitting.

CONCLUSION

We have described the direct fabrication of gC_3N_4-wrapped TNA heterojunctions via a chemical vapor deposition-like process by taking advantage of the pyrolysis of melamine to form gC_3N_4 that then is quickly deposited on the surface of TNAs. The gC_3N_4-wrapped TNA heterojunctions show excellent water splitting at a neutral medium. Precisely, such a gC_3N_4-wrapped TNA heterojunction has a current density of 224 $\mu A/cm^2$ at 0.6 V vs. Ag/AgCl, which is 16 times higher than that of the TNAs. This enhancement originates from forming an interface between gC_3N_4 and TNAs, accelerating the photo-response of this heterojunction under visible light.

ACKNOWLEDGEMENTS

The authors thank Ms. Pham Thi Kieu Oanh for the initial experimental setting of this study. This research is funded by the HUTECH University under grant number 63/HĐ-ĐKC (2019/02/19/CNC).

NOTES

The authors declare no competing financial interest.

SUPPORTING INFORMATION

Additional information as noted in the text. This information is available via the Internet at http://www.springer.com/chemistry/journal/11814.

REFERENCES

1. G. Dolf, B. Francisco and S. Deger, *Nat. Mater.*, **15**, 117 (2016).
2. S. Chu, Y. Cui and N. Liu, *Nat. Mater.*, **16**, 16 (2016).
3. S. Chu and A. Majumdar, *Nature*, **488**, 294 (2012).
4. M. G. Walter, E. L. Warren, J. R. McKone, S. W. Boettcher, Q. Mi, E. A. Santori and N. S. Lewis, *Chem. Rev.*, **110**, 6446 (2010).
5. C. Jiang, S. J. A. Moniz, A. Wang, T. Zhang and J. Tang, *Chem. Soc. Rev.*, **46**, 4645 (2017).
6. B. Liu, C. H. Kuo, J. Chen, Z. Luo, S. Thanneeru, W. Li, W. Song, S. Biswas, S. L. Suib and J. He, *Angew. Chem. Int. Ed.*, **54**, 9061 (2015).
7. R. R. Rao, M. J. Kolb, N. B. Halck, A. F. Pedersen, A. Mehta, H. You, K. A. Stoerzinger, Z. Feng, H. A. Hansen, H. Zhou, L. Giordano, J. Rossmeisl, T. Vegge, I. Chorkendorff, I. E. L. Stephens and Y. Shao-Horn, *Energy Environ. Sci.*, **10**, 2626 (2017).
8. P. Jiang, J. Chen, C. Wang, K. Yang, S. Gong, S. Liu, Z. Lin, M. Li, G. Xia, Y. Yang, J. Su and Q. Chen, *Adv. Mater.*, **30** (2018).
9. L. Fu, F. Yang, G. Cheng and W. Luo, *Nanoscale*, **10**, 1892 (2018).
10. E. Khorashadizade, S. Mohajernia, S. Hejazi, H. Mehdipour, N. Naseri, O. Moradlou, A. Z. Moshfegh and P. Schmuki, *J. Phys. Chem. C*, **125**, 6116 (2021).
11. X. Zhou, I. Hwang, O. Tomanec, D. Fehn, A. Mazare, R. Zboril, K. Meyer and P. Schmuki, *Adv. Funct. Mater.*, **31**, 2102843 (2021).
12. L. Zhuang, L. Ge, Y. Yang, M. Li, Y. Jia, X. Yao and Z. Zhu, *Adv. Mater.*, **29** (2017).
13. X. Li, W. Bi, L. Zhang, S. Tao, W. Chu, Q. Zhang, Y. Luo, C. Wu and Y. Xie, *Adv. Mater.*, **28**, 2427 (2016).
14. C. Ling, L. Shi, Y. Ouyang, X. C. Zeng and J. Wang, *Nano Lett.*, **17**, 5133 (2017).
15. C. Zhu, Q. Shi, S. Feng, D. Du and Y. Lin, *ACS Energy Lett.*, **3**, 1713 (2018).
16. J. Zhang, C. Liu and B. Zhang, *Small Methods*, **3**, 1800481 (2019).
17. W. H. Lai, L. F. Zhang, W. B. Hua, S. Indris, Z. C. Yan, Z. Hu, B. Zhang, Y. Liu, L. Wang, M. Liu, R. Liu, Y. X. Wang, J. Z. Wang, Z. Hu, H. K. Liu, S. L. Chou and S. X. Dou, *Angew. Chem. Int. Ed.*, **58**, 11868 (2019).
18. X. Zheng, J. Tang, A. Gallo, J. A. Garrido Torres, X. Yu, C. J. Athanitis, E. M. Been, P. Ercius, H. Mao, S. C. Fakra, C. Song, R. C. Davis, J. A. Reimer, J. Vinson, M. Bajdich and Y. Cui, *Proc. Natl. Acad. Sci. USA*, **118** (2021).
19. X. Li, S. Zhao, X. Duan, H. Zhang, S.-z. Yang, P. Zhang, S. P. Jiang, S. Liu, H. Sun and S. Wang, Appl. *Catal. B*, **283**, 119660 (2021).
20. A. Alarawi, V. Ramalingam and J.-H. He, *Mater. Today Energy*, **11**, 1 (2019).
21. Q. Wang, Z. Zhang, C. Cai, M. Wang, Z. L. Zhao, M. Li, X. Huang, S. Han, H. Zhou, Z. Feng, L. Li, J. Li, H. Xu, J. S. Francisco and M. Gu, *J. Am. Chem. Soc.*, **143**, 13605 (2021).
22. F. Fu, Z. Wu, G. Cha and P. Schmuki, *Chem. Commun.*, **57**, 7120 (2021).
23. J. H. Park, S. Kim and A. J. Bard, *Nano Lett.*, **6**, 28 (2006).

24. I. S. Cho, J. Choi, K. Zhang, S. J. Kim, M. J. Jeong, L. Cai, T. Park, X. Zheng and J. H. Park, *Nano Lett.*, **15**, 5709 (2015).
25. Z. Zhang, M. F. Hossain and T. Takahashi, *Int. J. Hydrogen Energy*, **35**, 8528 (2010).
26. S. Liang, J. He, Z. Sun, Q. Liu, Y. Jiang, H. Cheng, B. He, Z. Xie and S. Wei, *J. Phys. Chem. C*, **116**, 9049 (2012).
27. X. Cheng, Y. Zhang and Y. Bi, *Nano Energy*, **57**, 542 (2019).
28. Q.-q. Meng, J.-g. Wang, Q. Xie, H.-q. Dong and X.-n. Li, *Catal. Today*, **165**, 145 (2011).
29. J. Gong, Y. Lai and C. Lin, *Electrochim. Acta*, **55**, 4776 (2010).
30. X. Fan, J. Fan, X. Hu, E. Liu, L. Kang, C. Tang, Y. Ma, H. Wu and Y. Li, *Ceram. Int.*, **40**, 15907 (2014).
31. Y. Lai, J. Gong and C. Lin, *Int. J. Hydrogen Energy*, **37**, 6438 (2012).
32. S. W. Shin, J. Y. Lee, K.-S. Ahn, S. H. Kang and J. H. Kim, *J. Phys. Chem. C*, **119**, 13375 (2015).
33. H. Cui, W. Zhao, C. Yang, H. Yin, T. Lin, Y. Shan, Y. Xie, H. Gu and F. Huang, *J. Mater. Chem. A*, **2**, 8612 (2014).
34. Z. Li, H. Bian, X. Xiao, J. Shen, C. Zhao, J. Lu and Y. Y. Li, *ACS Appl. Nano Mater.*, **2**, 7372 (2019).
35. Y. Yin, Z. Jin and F. Hou, *Nanotechnology*, **18**, 495608 (2007).
36. J. Lin, Y. Liu, Y. Liu, C. Huang, W. Liu, X. Mi, D. Fan, F. Fan, H. Lu and X. Chen, *ChemSusChem*, **12**, 961 (2019).
37. Q. Gui, Z. Xu, H. Zhang, C. Cheng, X. Zhu, M. Yin, Y. Song, L. Lu, X. Chen and D. Li, *ACS Appl. Mater. Interfaces*, **6**, 17053 (2014).
38. J. Luo, Y. Ma, H. Wang and J. Chen, *Electrochim. Acta*, **167**, 119 (2015).
39. X. Lu, Z. Liu, J. Li, J. Zhang and Z. Guo, *Appl. Catal. B*, **209**, 657 (2017).
40. B. Rhimi, C. Wang and D. W. Bahnemann, *J. Phys. Energy*, **2**, 042003 (2020).
41. P. V. Viet, N. H. Phuong, T. H. Huy, B. D. Phat, L. V. Hai, P. M. Thuan, S. J. You and C. M. Thi, *J. Sci.-Adv. Mater. Dev.*, **17**, 2101070 (2021).
42. Q. Zhu, Z. Xu, B. Qiu, M. Xing and J. Zhang, *Small*, **6**, 551 (2021).
43. L. Wang, Y. Tong, J. Feng, J. Hou, J. Li, X. Hou and J. Liang, *SM&T*, **19**, 00089 (2019).
44. Y. Hou, Z. Wen, S. Cui, X. Feng and J. Chen, *Nano Lett.*, **16**, 2268 (2016).
45. L. Xiao, T. Liu, M. Zhang, Q. Li and J. Yang, *ACS Sustain. Chem. Eng.*, **7**, 2483 (2018).
46. W. Kong, X. Zhang, B. Chang, Y. Zhou, S. Zhang, G. He, B. Yang and J. Li, *Electrochim. Acta*, **282**, 767 (2018).
47. C. Liu, F. Wang, J. Zhang, K. Wang, Y. Qiu, Q. Liang and Z. Chen, *Nanomicro. Lett.*, **10**, 37 (2018).
48. C. Pan, J. Xu, Y. Wang, D. Li and Y. Zhu, *Adv. Funct. Mater.*, **22**, 1518 (2012).
49. W. Ma, D. Han, M. Zhou, H. Sun, L. Wang, X. Dong and L. Niu, *Chem. Sci.*, **5**, 3946 (2014).
50. M. Wang, S. Dipazir, P. Lu, Y. Wang, M. Yuan, S. Li and G. Zhang, *J. Colloid Interface Sci.*, **532**, 774 (2018).
51. B. Zhang, C. Xiao, S. Xie, J. Liang, X. Chen and Y. Tang, *Chem. Mater.*, **28**, 6934 (2016).
52. D. Liu, Q. Lu, Y. Luo, X. Sun and A. M. Asiri, *Nanoscale*, **7**, 15126 (2015).
53. A. Sivanantham, P. Ganesan and S. Shanmugam, *Adv. Funct. Mater.*, **26**, 4661 (2016).
54. N. T. Tho, C. M. Thi, L. V. Hieu and P. V. Viet, *J. Aust. Ceram. Soc.*, **56**, 849 (2019).
55. O. Almora, C. Aranda, E. Mas-Marzá and G. Garcia-Belmonte, *Appl. Phys. Lett.*, **109**, 173903 (2016).
56. P. V. Viet, T. H. Huy, N. X. Sang, C. M. Thi and L. V. Hieu, *J. Mater. Sci.*, **53**, 3364 (2017).
57. P. V. Viet, B. D. Phat, T. H. Huy, C. M. Thi, N. T. Khoa, K. Y. Soo and L. V. Hieu, *RSC Adv.*, **8**, 12420 (2018).
58. S. Singh, V. Sharma and K. Sachdev, *J. Mater. Sci.*, **52**, 11580 (2017).
59. D. Jiang, X. Sun, H. Zhang, K. Wang, L. Shi and F. Du, *Appl. Phys. A*, **126** (2020).
60. A. Ghobadi, T. G. Ulusoy, R. Garifullin, M. O. Guler and A. K. Okyay, *Sci. Rep.*, **6**, 30587 (2016).
61. W. Zhang, L. Zhou and H. Deng, *J. Mol. Catal. A Chem.*, **423**, 270 (2016).
62. L. P. P. Ha, T. H. T. Vinh, N. T. B. Thuy, C. M. Thi and P. V. Viet, *J. Environ. Chem. Eng.*, **9**, 105103 (2021).
63. T. K. Thao, N. Q. Thang, L. P. P. Ha, L. V. Hai, T. V. Man, C. M. Thi and P. V. Viet, *Chemosphere*, **268**, 129291 (2021).
64. F. E. Bedoya Lora, A. Hankin and G. H. Kelsall, *J. Mater. Chem. A*, **5**, 22683 (2017).
65. M. Sun, Y. Fang, Y. Kong, S. Sun, Z. Yu and A. Umar, *J. Chem. Soc., Dalton Trans.*, **45**, 12702 (2016).
66. D. Zhou, Z. Chen, Q. Yang, C. Shen, G. Tang, S. Zhao, J. Zhang, D. Chen, Q. Wei and X. Dong, *ChemCatChem*, **8**, 3064 (2016).
67. B. Pandey, S. Rani and S. C. Roy, *J. Alloys Compd.*, **846**, 155881 (2020).
68. B. Chai, T. Peng, J. Mao, K. Li and L. Zan, *Phys. Chem. Chem. Phys.*, **14**, 16745 (2012).
69. C. Pan, J. Jia, X. Hu, J. Fan and E. Liu, *Appl. Surf. Sci.*, **430**, 283 (2018).
70. B. Rezaei, N. Irannejad and A. A. Ensafi, *Renew. Energy*, **123**, 281 (2018).
71. T. H. Huy, D. P. Bui, F. Kang, Y. F. Wang, S. H. Liu, C. M. Thi, S. J. You, G. M. Chang and P. V. Viet, *Chemosphere*, **215**, 323 (2019).